

ARMY RESEARCH LABORATORY



Performance of Acoustic Tracking Arrays in Atmospheric Turbulence

by David Keith Wilson

ARL-TR-1286

July 1997

DTIC QUALITY INSPECTED 2

19970730 116

Approved for public release; distribution unlimited.

The findings in this report are not to be construed as an official Department of the Army position unless so designated by other authorized documents.

Citation of manufacturer's or trade names does not constitute an official endorsement or approval of the use thereof.

Destroy this report when it is no longer needed. Do not return it to the originator.

Army Research Laboratory

Adelphi, MD 20783-1197

ARL-TR-1286

July 1997

Performance of Acoustic Tracking Arrays in Atmospheric Turbulence

David Keith Wilson

Information Science Technology Directorate

Approved for public release; distribution unlimited.

Abstract

A method is described for assessing the performance of acoustic arrays used to determine source bearings. The method involves calculation of the Cramer-Rao lower bound (CRLB), which characterizes the best performance obtainable for a given array configuration and set of operating conditions. The CRLB calculations are used to show that the performance of the arrays depends on the sensor configuration, the acoustic frequency, the distance from the source, the background noise, and atmospheric turbulence. Near to the source, and at low frequencies, it is the background noise that limits array performance. Turbulence becomes the limiting factor as the distance and frequency are increased. When performance is limited by turbulence, the calculations are found to be very sensitive to the particular turbulence model used. The von Kármán type of model appears to provide the most reasonable CRLB calculations. The turbulent degradation is found to result primarily from small-scale fluctuations in the wind velocity. Performance predictions for ARL's Remote Netted Acoustic Detection System (RNADS) are presented; it is found that RNADS should provide angle-of-arrival (AOA) accuracy of several degrees or better for signal-to-noise ratios above 10 dB during most atmospheric turbulence conditions.

Contents

1	Introduction	1
2	General Matrix Formulation	3
2.1	<i>Angle of Arrival versus Bearing</i>	3
2.2	<i>Sensor Cross-Correlation Analysis</i>	4
2.3	<i>Wavefront Phase Delays</i>	5
2.4	<i>Assessment of Array Performance</i>	6
2.4.1	Example 1: Two-Element Array	8
2.4.2	Example 2: Triangular Array	9
3	Incorporation of Turbulence Effects	11
3.1	<i>Effective Index-of-Refraction Fluctuation</i>	11
3.2	<i>Mutual Coherence Function</i>	12
3.3	<i>Turbulence Models</i>	12
3.4	<i>Modification of Signal Correlation Matrix</i>	14
4	Example Calculations and Discussion	17
4.1	<i>Long Baseline—Sensor Decorrelation Trade-Off</i>	17
4.2	<i>Dependence of Array Performance on Meteorological Conditions</i>	17
4.3	<i>Calculations for Circular RNADS Array</i>	23
5	Conclusions	26
6	Recommendations	27
A	Statistical Turbulence Models	29
A-1.	<i>Correlation and Spectral Functions</i>	29
A-2.	<i>Energy Spectra</i>	30
A-3.	<i>Length Scales</i>	31
A-4.	<i>Gaussian Model</i>	32
A-5.	<i>Von Kármán Model</i>	33
	References	35
	Acronyms	37
	Distribution	39
	Report Documentation Page	43

Figures

1	Partial listing of current generation of acoustical systems used to track sources on battlefield	1
2	Deployment of acoustical array for tracking target	1
3	Effect of refraction on angle of arrival of acoustic wavefronts	3
4	Planar wavefronts incident on pair of receivers	5
5	Polar plot of Cramer-Rao lower bounds for AOA estimations	10
6	Comparison of transverse correlation functions for different turbulence models	15
7	Comparison of mutual coherence functions for several different turbulence models	15
8	Mutual coherence function for several values of $k^2 x \mathcal{L}$	15
9	Effect of changing sensor spacing on AOA estimation errors: moderate noise, von Kármán turbulence model case	18
10	Effect of changing sensor spacing on AOA estimation errors: low noise, von Kármán turbulence model	18
11	Effect of changing sensor spacing on AOA estimation errors: low noise, Gaussian turbulence model	18
12	Two-dimensional correlation function (TCF) for convective, atmospheric boundary layer conditions	20
13	TCF difference function $b_{eff}(0) - b_{eff}(\rho)$ for convective boundary layer conditions	21
14	TCF difference function $b_{eff}(0) - b_{eff}(\rho)$ for nearly neutral conditions	22
15	TCF difference function $b_{eff}(0) - b_{eff}(\rho)$ for calm boundary layer conditions	22
16	MCF calculations as a function of turbulence conditions	22
17	CRLB as a function of turbulence conditions, for a five-element line array at parallel incidence	23
18	Sensor layout for circular RNADS array in a horizontal plane	24
19	CRLB for circular RNADS array in convective atmospheric boundary layer, low-noise case	24
20	CRLB for circular RNADS array in convective atmospheric boundary layer, high-noise case	25
21	CRLB for circular RNADS array in neutral atmospheric boundary layer, low-noise case	25
22	CRLB for circular RNADS array in calm atmospheric boundary layer, low-noise case	25
A-1	Comparison of Gaussian and von Kármán energy spectral models	33

1. Introduction

Acoustic sensor arrays can be used to detect, locate, and classify targets in atmospheric battlespaces. Their main advantages, in comparison to radar and optical systems, are low cost, functionality in non-line-of-sight situations, and insusceptibility to simple countermeasures (Srouer and Robertson, 1995). These advantages help explain why acoustical systems have achieved a surge in popularity in recent years; some of these new acoustical systems are listed in figure 1. The deployment of an acoustical array for target tracking is illustrated in figure 2. The operational principle is to use the phase differences between the signals recorded at the individual microphones to determine the orientation of the wavefronts, which corresponds to the bearing of the target.

Acoustical systems are not without shortcomings. Most importantly, the performance of acoustical arrays depends strongly on meteorological conditions. It is normally enhanced by still, nighttime conditions. On the other hand, the atmospheric turbulence characteristic of windy conditions or a sunny day can cause significant degradation. This is because array beam-forming depends on good mutual coherence of the signals received by the individual sensors; turbulence causes a loss of such coherence.

Despite the recent popularity of acoustical arrays and the importance of atmospheric turbulence in determining the performance of these systems, so far little effort has been devoted to quantifying the turbulence effects.

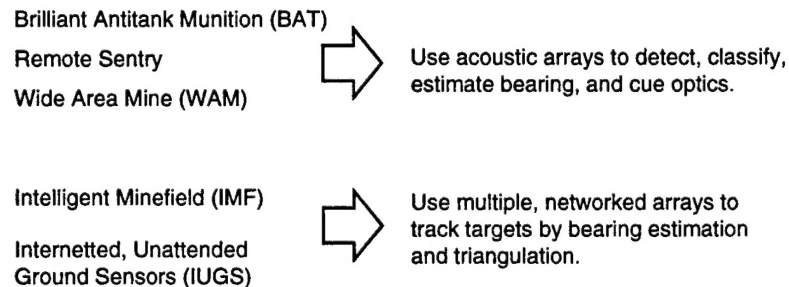


Figure 1: Partial listing of current generation of acoustical systems used to track sources on battlefield.

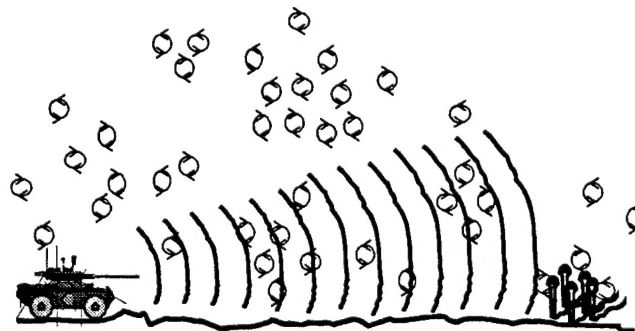


Figure 2: Deployment of acoustical array for tracking target. Phase information at microphones is used to determine orientation of incoming sound wavefronts. Turbulence causes random fluctuations in wavefront orientation.

In order to place the previous research in perspective, it is helpful to break down the general topic of turbulence effects on acoustic sensor arrays into two subtopics: first, the effect of turbulence on reducing the mutual coherence between a single pair of microphones, as a function of their separation; and second, the statistical analysis of the performance of a full array, given knowledge of the coherence.

Some of the earliest work on coherence is summarized by Tatarskii (1961, 1971). Tatarskii's theoretical treatment has served as the basis for most subsequent work throughout the acoustical spectrum. The main difficulty with Tatarskii's theory is its inapplicability to large-scale turbulence (i.e., eddy sizes larger than several meters), which has a complicated anisotropic and inhomogeneous structure. Acoustical systems that operate in frequency ranges of several hundred hertz and lower are strongly affected by large-scale turbulence.

Tatarskii also described some experimental evidence for his treatment of coherence, although the studies he considered dealt mostly with ultrasonic frequencies, which are less sensitive to large-scale turbulence structure. Experimental studies on the coherence of audible-range sound waves have been performed during recent decades by Daigle *et al.* (1983) and Havelock *et al.* (1995).

The second topic mentioned above, the statistical analysis of array performance, has apparently not been addressed previously for a turbulent atmosphere. Song and Ritcey (1996), however, do consider the performance of acoustic arrays in a randomly fluctuating ocean. Their analysis applies quite well to the atmospheric case, so long as the statistical model used for the fluctuations is appropriate to the atmosphere. The analysis in this report is derived in part from Song and Ritcey's.

Section 2 provides a statistical formulation of array performance. A matrix representation for the sensor cross correlations is employed to cast the equations in a particularly simple format. Modeling of turbulence effects on the signal coherence is discussed in section 3. Section 4 presents example assessments of array performance for realistic meteorological conditions. Among the array configurations considered is the one used by the Army Research Laboratory (ARL) Remote Netted Acoustic Detection System (RNADS) (Srouf and Robertson, 1995). RNADS is fairly representative of the acoustical systems listed in figure 1.

It will become clear from many of the example calculations in this report that accurate assessments of acoustic array performance require careful attention to modeling of atmospheric turbulence. Therefore, I include some of the relevant turbulence modeling issues and mathematics in an appendix.

2. General Matrix Formulation

2.1 Angle of Arrival versus Bearing

The analysis described in this section is for two-dimensional sensor arrays. Three-dimensional arrays can, of course, also be built and analyzed; we gain little physical insight, however, by introducing this additional complication.

A two-dimensional array can be used to determine the bearing of a source only in the plane of the array. For example, if the array is horizontal, it can be used to determine only the azimuthal bearing of the source. A vertical array would determine the elevation angle. Most of the analysis in this section applies equally well to horizontal and vertical arrays. However, there are practical reasons why most acoustical systems designed for the battlefield are horizontal arrays, rather than vertical ones. The most important of these is *refraction*, as illustrated in figure 3. Refraction by atmospheric wind and temperature gradients causes the orientation of the wavefronts to gradually change. Eventually, there may be little resemblance between the angle of arrival of the wavefronts and the actual bearing of the source.

When propagation is upwind (or the temperature increases with height), sound is refracted downward. As a result, there can be a "multipath effect": i.e., multiple wavefronts and angles of arrival. When propagation is downwind (or the temperature decreases with height), sound is refracted upward. Most of the sound energy reaching the receivers is normally scattered there by turbulence. As a result, the angle of arrival has more to do with the location of the dominant scattering volume than the actual bearing of the source.

Fortunately, horizontal refraction is minimal in comparison to vertical refraction. Hence we need not worry about this complication if we are interested only in horizontal arrays. It is worth pointing out, however, that if

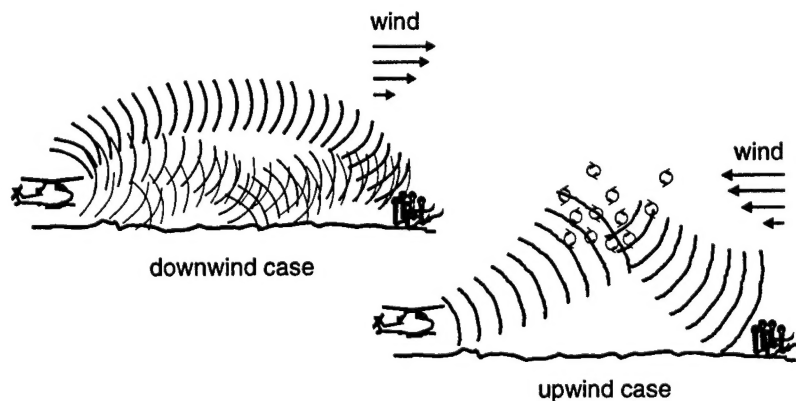


Figure 3: Effect of refraction on angle of arrival of acoustic wavefronts. As result of refraction, actual bearing of source can differ from angle of arrival.

we have access to propagation models that can determine vertical refractive effects sufficiently well, it should be possible to build vertical arrays that accurately track the elevation of targets. In the remaining part of this section, I circumvent the issue of refraction by referring to the accuracy of angle-of-arrival (AOA) estimates for the acoustic wavefronts, as opposed to the actual angle of bearing (AOB) of the source. The distinction between AOA and AOB is of little practical significance for horizontal tracking arrays, but should be kept in mind for vertical tracking arrays.

2.2 Sensor Cross-Correlation Analysis

Consider a planar array of N sensors. The signal at each of the sensors is assumed to have two contributions: one that has propagated through the atmosphere from a source and arrived at the array with wavefront normal angle ψ , and the second consisting of random noise. These two contributions are indicated by $\mathbf{s}(\psi, t)$ and $\mathbf{n}(t)$, respectively. The signals are represented in complex notation, as is common in acoustics and wave propagation generally. (See, for example, Kinsler *et al.* (1982) or sect. 6.9 in Burdic (1984). The complex part of the signal may be regarded as the Hilbert transform of the real signal.) Boldface is used here to indicate matrices; $\mathbf{s}(\psi, t)$ and $\mathbf{n}(t)$ are column vectors having N elements, each element corresponding to the signal received by one of the sensors. The source contributions vary in time owing to the effect of random turbulent fluctuations on the propagation.* The noise contributions may be from the wind or other acoustic sources on the battlefield.

The total received signal is

$$\mathbf{p}(\psi, t) = \mathbf{s}(\psi, t) + \mathbf{n}(t). \quad (2.1)$$

The cross correlations between the sensor signals can be written compactly in matrix form as

$$\mathbf{R}_{pp}(\psi) = \langle \mathbf{p}(\psi, t) \tilde{\mathbf{p}}(\psi, t) \rangle, \quad (2.2)$$

where the angle brackets indicate the ensemble average, and the tilde is the conjugate transpose. Assuming that the source signal and noise are uncorrelated,

$$\mathbf{R}_{pp}(\psi) = \mathbf{R}_{ss}(\psi) + \mathbf{R}_{nn}(\psi). \quad (2.3)$$

Assuming furthermore that the noise at the sensors is mutually uncorrelated and equal in variance, we can write

$$\mathbf{R}_{pp}(\psi) = \mathbf{R}_{ss}(\psi) + \sigma_n^2 \mathbf{I}, \quad (2.4)$$

*Of course, the source signal may vary in time for other reasons. For example, its bearing and distance may change as a result of source motion, or its spectral content may change as a result of mechanical operations (e.g., a tank accelerating). Although such complications can be significant, I do not consider them in this report in order to preserve the focus on turbulence effects.

where σ_n^2 is the noise variance. It is convenient to normalize the signals and noise so that $\mathbf{s}(\psi, t)$ has unit variance. Then σ_n^2 becomes a noise-to-signal variance ratio. The signal-to-noise ratio (SNR) in decibels is defined as

$$\text{SNR} = -10 \log \sigma_n^2. \quad (2.5)$$

2.3 Wavefront Phase Delays

Realistic modeling of $\mathbf{R}_{ss}(\psi)$ is rather difficult. While this correlation matrix depends most importantly on the relative sensor positions, it also depends on several other factors that affect the propagation, such as turbulence, refraction, and absorption of sound by air. I consider the turbulence effects in section 3; for now, I formulate $\mathbf{R}_{ss}(\psi)$ assuming perfect plane-wave propagation. This sort of formulation is valid if the dimensions of the array are small compared to its distance from the source.

Assuming perfect plane-wave propagation, the elements of $\mathbf{R}_{ss}(\psi)$ depend only on the relative phase delays between the incidence of the acoustic wavefronts at the receivers. The situation is shown, for two sensors, in figure 4.

In the figure, one sensor is at the origin, while the second is at (x, y) . The AOB of the second sensor is $\alpha = \arctan(y/x)$. Suppose there are plane waves incident on the sensors, having an orientation angle β . Note that $\beta = \psi - \pi/2$, ψ being the angle of the wavefront normal. The distance between the receivers, projected onto the wavefront normal, is $d_\lambda = d \sin(\beta - \alpha)$, where $d^2 = x^2 + y^2$. Therefore, the phase delay between wavefront incidence at the two receivers is $kd_\lambda = kd \sin(\beta - \alpha) = -kd \cos(\psi - \alpha)$, where $k = 2\pi/\lambda$ is the wavenumber. The signal at sensor two is equal to the signal at sensor one times the phase factor $\exp(ikd_\lambda)$.

The same geometrical arguments hold when multiple receivers are considered. The phase delay between sensors m and n is, therefore,

$$S_{mn}(\psi) = \exp[-ikd_{mn} \cos(\psi - \alpha_{mn})], \quad (2.6)$$

where

$$d_{mn}^2 = (x_n - x_m)^2 + (y_n - y_m)^2,$$

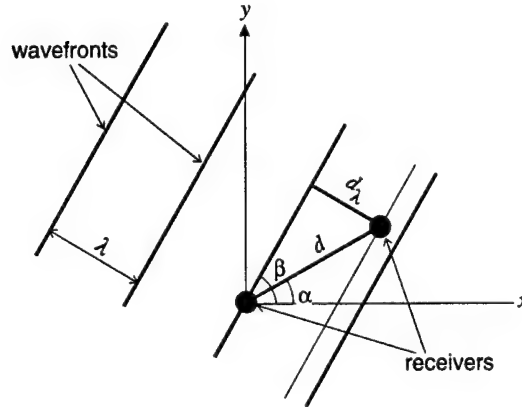


Figure 4: Planar wavefronts incident on pair of receivers.

and

$$\alpha_{mn} = \arctan [(y_n - y_m) / (x_n - x_m)].$$

The matrix formed from the phase delays, $\mathbf{S}(\psi)$, is generally referred to as the *array steering matrix*. In the nonturbulent case, $\mathbf{R}_{ss}(\psi) = \mathbf{S}(\psi)$. I show in section 3, however, that this simple relationship no longer holds when turbulence is considered.

2.4 Assessment of Array Performance

We can quantify the performance of the sensor array by calculating the mean square error (mse) $\langle (\psi - \hat{\psi})^2 \rangle$, where $\hat{\psi}$ is the estimated AOA. By way of an introduction, I calculate the mse for a simple example: an array of two sensors separated by a distance d .

Suppose there are two sensors on the y -axis at $y = -d/2$ and $y = +d/2$. If we take the phase at the sensor at $y = +d/2$ as the reference phase, equation (2.1) becomes for this case

$$\begin{bmatrix} p_1 \\ p_2 \end{bmatrix} = \begin{bmatrix} 1 \\ e^{-ikd \cos(\psi - \pi/2)} \end{bmatrix} + \begin{bmatrix} n_1 \\ n_2 \end{bmatrix} = \begin{bmatrix} 1 \\ e^{-ikd \sin \psi} \end{bmatrix} + \begin{bmatrix} n_1 \\ n_2 \end{bmatrix}.$$

When there is no noise, we can determine ψ *exactly* from the phase difference $\Delta\phi$ between p_1 and p_2 :

$$\Delta\phi = \angle p_1 - \angle p_2 = \angle (p_1 p_2^*) = kd \sin \psi,$$

and hence

$$\psi = \arcsin \left(\frac{\Delta\phi}{kd} \right). \quad (2.7)$$

(The asterisk denotes the complex conjugate.) When noise is present, it is natural to estimate ψ by averaging several samples of $\Delta\phi = \angle (p_1 p_2^*)$. It can be shown that the real and imaginary parts of $p_1 p_2^*$ are

$$\Re [p_1 p_2^*] = \cos \alpha + n_{2x} + n_{1x} \cos \alpha + n_{1y} \sin \alpha + n_{1x} n_{2x} + n_{1y} n_{2y}, \quad (2.8)$$

$$\Im [p_1 p_2^*] = -\sin \alpha - n_{2y} + n_{1y} \cos \alpha - n_{1x} \sin \alpha - n_{1x} n_{2y} + n_{1y} n_{2x}, \quad (2.9)$$

where $\alpha = -kd \sin \psi$, $n_{jx} = \Re [n_j]$, and $n_{jy} = \Im [n_j]$. Note that the variance of n_{jx} and n_{jy} must individually be $\sigma_n^2/2$, in order for the variance of n_j to be equal to σ_n^2 .

It is not possible to derive closed-form results for $\hat{\psi}$ from equations (2.8) and (2.9) in general. However, if we suppose that σ_n^2 , kd , and ψ are all much less than one (i.e., low noise, small separation compared to the wavelength, and near broadside incidence), we have

$$\Re [p_1 p_2^*] \simeq 1 + n_{2x} + n_{1x},$$

$$\Im[p_1 p_2^*] \simeq -\alpha - n_{2y} + n_{1y}.$$

Hence the phase angle $\Delta\phi$ is approximately

$$\begin{aligned}\Delta\phi &\simeq \arctan\left(\frac{-\alpha - n_{2y} + n_{1y}}{1 + n_{2x} + n_{1x}}\right) \\ &\simeq (-\alpha - n_{2y} + n_{1y})(1 - n_{2x} - n_{1x}) \\ &\simeq -\alpha - n_{2y} + n_{1y} \\ &\simeq kd\psi - n_{2y} + n_{1y}.\end{aligned}$$

We find the estimated AOA $\hat{\psi}$ by averaging several (M) samples of $\Delta\phi$ and dividing by kd :

$$\hat{\psi} = \psi + \frac{1}{M} \sum_{m=1}^M \frac{n_{1y}^m - n_{2y}^m}{kd},$$

where the superscripts m indicate statistically independent samples of the noise. The mse can now be calculated:

$$\begin{aligned}\left\langle (\psi - \hat{\psi})^2 \right\rangle &= \frac{1}{(kdM)^2} \left\langle \left[\sum_{m=1}^M (n_{1y}^m - n_{2y}^m)^2 \right] \right\rangle \\ &= \frac{1}{(kdM)^2} 2M (\sigma_n^2/2) \\ &= \frac{1}{M (kd)^2}.\end{aligned}\tag{2.10}$$

For most array geometries and processing methods, it is unfortunately impossible to calculate the mse in closed form. Fortunately, it is possible to perform calculations on a computer that give useful information on the mse. A particularly useful characterization of the mse is provided by the *Cramer-Rao theorem*. According to this theorem, the *minimum* mse is the inverse of the Fisher information matrix $\mathbf{J}(\psi)$ (Scharf, 1991):

$$\left\langle (\psi - \hat{\psi})^2 \right\rangle \geq \mathbf{J}^{-1}(\psi).\tag{2.11}$$

The right-hand side of equation (2.11) is called the *Cramer-Rao lower bound* (CRLB). In our case, since we have only one parameter to be determined, ψ , the information matrix is actually a scalar. (For multiple sources, the information matrix would have multiple elements.) Song and Ritcey (1996) show, for signals having a joint-Gaussian probability distribution, that

$$\mathbf{J}(\psi) = M \operatorname{tr} \left(\mathbf{R}_{pp}^{-1} \frac{\partial \mathbf{R}_{pp}}{\partial \psi} \mathbf{R}_{pp}^{-1} \frac{\partial \mathbf{R}_{pp}}{\partial \psi} \right).\tag{2.12}$$

In the above, $\operatorname{tr}()$ is the trace of the matrix, and M is the number of statistically independent samples used to estimate the correlation matrix of $\mathbf{p}(\psi, t)$.

It must be kept in mind that the Cramer-Rao theorem gives the *minimum* possible error. Since noise and turbulence effects on the propagation are random, the *actual* error is also random. The error furthermore depends on what

method is used to estimate the AOA. Among the more common methods are sum-difference beamforming, the Bartlett beamformer, and maximum-likelihood estimation. The essential task to be accomplished is this: given a number of independent samples of $\mathbf{p}(\psi, t)$ collected at a discrete set of times t_m , and a theoretical model for $\mathbf{R}_{pp}(\psi)$, we desire an estimate for ψ . Most methods involve estimating the correlation matrix of $\mathbf{p}(\psi, t)$ from the actual measurements. For example, the following matrix may be computed:

$$\mathbf{C}_{pp} = \frac{1}{M} \sum_{m=1}^M \mathbf{p}(\psi, t_m) \tilde{\mathbf{p}}(\psi, t_m).$$

Given enough independent samples, we would expect \mathbf{C}_{pp} to converge to \mathbf{R}_{pp} . The reason the number of samples M appears in the calculation of the Fisher information matrix is that the fidelity of the estimate \mathbf{C}_{pp} improves with more data, so that the estimate of the AOA is improved.

For the acoustic array performance evaluations given in this report, I provide only calculations of the CRLB. The calculated errors are therefore intrinsically optimistic assessments of actual array performance. However, it is worth pointing out that Song and Ritcey (1996), in their calculations of turbulence effects on AOA estimates, were able to achieve performance very near the CRLB using the maximum-likelihood method. Therefore, the CRLB calculations are useful.

In most of the remainder of this report, when I speak of the CRLB, I actually mean its square root. Since the square root has linear dimensions (in degrees), it is more intuitive to deal with than the actual CRLB (in units of degrees squared). The square root of the CRLB can be thought of as a lower bound on the standard deviation of the measurement error.

2.4.1 Example 1: Two-Element Array To illustrate the CRLB analysis, I return to the simple example considered earlier: that of two sensors separated by a distance d . In matrix form, the product of the wavenumber and sensor spacings is

$$[kd_{mn}] = \begin{bmatrix} 0 & kd \\ kd & 0 \end{bmatrix}.$$

The relative angles between the sensors are

$$[\alpha_{mn}] = \begin{bmatrix} 0 & \pi/2 \\ -\pi/2 & 0 \end{bmatrix}.$$

Hence, from equations (2.6) and (2.4),

$$\mathbf{R}_{pp}(\psi) = \begin{bmatrix} 1 + \sigma_n^2 & e^{-ikd \cos(\psi - \pi/2)} \\ e^{-ikd \cos(\psi + \pi/2)} & 1 + \sigma_n^2 \end{bmatrix},$$

which, using elementary trigonometric identities, we can simplify to

$$\mathbf{R}_{pp}(\psi) = \begin{bmatrix} 1 + \sigma_n^2 & e^{-ikd \sin \psi} \\ e^{ikd \sin \psi} & 1 + \sigma_n^2 \end{bmatrix}.$$

In order to calculate the CRLB, we still need the inverse of $\mathbf{R}_{pp}(\psi)$, as well as its derivative with respect to ψ (see eq (2.12)). The inverse of the matrix is simply

$$\mathbf{R}_{pp}^{-1}(\psi) = \frac{1}{\sigma_n^2(2 + \sigma_n^2)} \begin{bmatrix} 1 + \sigma_n^2 & -e^{-ikd \sin \psi} \\ -e^{ikd \sin \psi} & 1 + \sigma_n^2 \end{bmatrix},$$

and the derivative is

$$\frac{\partial \mathbf{R}_{pp}}{\partial \psi} = \begin{bmatrix} 0 & -ikd \cos \psi e^{-ikd \sin \psi} \\ ikd \cos \psi e^{ikd \sin \psi} & 0 \end{bmatrix}.$$

Multiplying these matrices, we have

$$\mathbf{R}_{pp}^{-1} \frac{\partial \mathbf{R}_{pp}}{\partial \psi} = \frac{ikd \cos \psi}{\sigma_n^2(2 + \sigma_n^2)} \begin{bmatrix} -1 & -(1 + \sigma_n^2) e^{-ikd \sin \psi} \\ (1 + \sigma_n^2) e^{ikd \sin \psi} & 1 \end{bmatrix},$$

and therefore

$$\text{tr} \left(\mathbf{R}_{pp}^{-1} \frac{\partial \mathbf{R}_{pp}}{\partial \psi} \mathbf{R}_{pp}^{-1} \frac{\partial \mathbf{R}_{pp}}{\partial \psi} \right) = \frac{2(kd)^2 \cos^2 \psi}{\sigma_n^2(2 + \sigma_n^2)}.$$

Hence the CRLB (eq (2.11)) is

$$\mathbf{J}^{-1}(\psi) = \frac{\sigma_n^2(2 + \sigma_n^2)}{2M(kd)^2 \cos^2 \psi}. \quad (2.13)$$

Clearly the two-element array performs best when the source is perpendicular to the array axis ($\psi = 0$). In fact, when the source is in a line with the receivers ($\psi = \pi/2$), the CRLB becomes singular. Note that equation (2.13) is equivalent to equation (2.10) if one makes the approximations $\sigma_n^2 \ll 1$ and $\psi \ll 1$. Also, the two-element array has a $\pm\pi$ ambiguity in the AOA estimation (e.g., it has no intrinsic way to distinguish $\psi = 0$ from $\psi = \pi$). The CRLB calculation actually assumes, implicitly, that this information is somehow available.

A polar plot of the CRLB is presented in figure 5 (solid line), for $\sigma_n^2 = 0.1$ and $d = \lambda/2$ ($kd = \pi$). The CRLB appears as two parallel lines when plotted in this manner.

2.4.2 Example 2: Triangular Array A more complicated case is that of an equilateral triangular array. With vertices at $(0, d/\sqrt{3})$, $(-d/2, -d/2\sqrt{3})$, and $(d/2, -d/2\sqrt{3})$, the sensor spacing matrix is

$$[kd_{mn}] = \begin{bmatrix} 0 & kd & kd \\ kd & 0 & kd \\ kd & kd & 0 \end{bmatrix}$$

and the angular orientation matrix is

$$[\alpha_{mn}] = \begin{bmatrix} 0 & -2\pi/3 & -\pi/3 \\ \pi/3 & 0 & \pi \\ 2\pi/3 & \pi & 0 \end{bmatrix}.$$

Hence,

$$\mathbf{R}_{pp}(\psi) = \begin{bmatrix} 1 + \sigma_n^2 & e^{-ikd \cos(\psi+2\pi/3)} & e^{-ikd \cos(\psi+\pi/3)} \\ e^{ikd \cos(\psi+2\pi/3)} & 1 + \sigma_n^2 & e^{-ikd \cos(\psi)} \\ e^{ikd \cos(\psi+\pi/3)} & e^{ikd \cos(\psi)} & 1 + \sigma_n^2 \end{bmatrix}.$$

Analytical calculation of the CRLB becomes extremely complicated for this case. It is rather simple, though, to compute numerical results with a matrix computation package such as Matlab[®]. Results for $d = \lambda/2$ are shown (dotted line) superimposed on the polar plot for the two-element line array (fig. 5).

The CRLB for an equilateral triangle is a circle, meaning that there are no preferred directions for detection. This is somewhat surprising: since the line array has two preferred directions, one might expect the triangular array to have three preferred directions. But all test cases that I have computed for regular polygons (such as a hexagon with side length $d = \lambda/2$, results for which are also shown in fig. 5, double-dash-dotted line) have yielded an omnidirectional CRLB. The underlying mathematical reasons for this are unclear to me. The CRLB calculation for a random configuration of three or more sensors, also shown in figure 5 (dotted line), yields an ellipsoidal response. (The ellipsoid depicted is a typical result; other random configurations yield ellipsoids having different orientations and axes.)

In connection with figure 5, it should be stressed that the calculations are for the CRLB, and not for actual phased-array beam patterns or for specific signal-processing algorithms. As discussed in section 2.2.4, the CRLB represents the theoretically best attainable performance. Only with good algorithms can one actually obtain similar results.

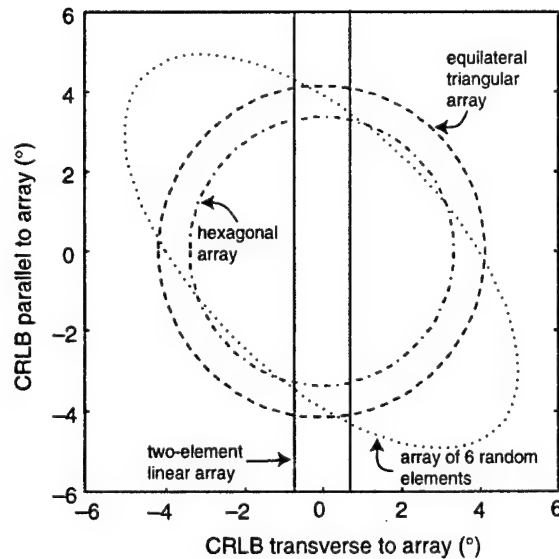


Figure 5: Polar plot of Cramer-Rao lower bounds for AOA estimations.

3. Incorporation of Turbulence Effects

Turbulence causes random fluctuations, in both phase and amplitude, of the received signals. These random fluctuations would not interfere with AOA estimation if they caused equal and synchronized fluctuations in phase and amplitude at all sensors. The problem is that the phase and amplitude fluctuations at the individual array elements are unsynchronized with one another. In this section, I explain how the effect of this imperfect coherence on the sensor array can be modeled.

3.1 Effective Index-of-Refractive Fluctuation

Turbulent fluctuations in air temperature, moisture, and wind velocity all affect acoustic propagation. Both the temperature and moisture fluctuations cause the acoustic index of refraction to fluctuate. Let us define the squared index of refraction as

$$\epsilon = n^2 - 1. \quad (3.1)$$

In the above, $n = c_0/c$ is the index of refraction, c being the actual sound speed and c_0 its ambient value. The speed of sound, in terms of the absolute temperature T and specific humidity q , is

$$c \simeq 20.02 \sqrt{T(1 + 0.62q)}.$$

Normally, the fluctuations in the sound speed, $c' = c - c_0$, are small compared to the ambient value. Therefore,

$$n^2 = \frac{c_0^2}{(c_0 + c')^2} \simeq \frac{c_0^2}{c_0^2 + 2c_0c'} \simeq 1 - \frac{2c'}{c_0}.$$

The squared index of refraction is then

$$\epsilon \simeq -\frac{2c'}{c_0}. \quad (3.2)$$

The effect of velocity fluctuations is similar to the effect of sound speed fluctuations. If we make a parabolic approximation to the acoustic wave equation, it can be shown that, in the presence of turbulent velocity fluctuations, ϵ can be replaced by the following effective value (Ostashev, 1994):

$$\epsilon_{eff} = \epsilon - 2u_1/c_0, \quad (3.3)$$

in which u_1 is the fluctuation of the velocity component parallel to the direction of propagation.

The statistical spatial structure of the effective index of refraction, and its effects on acoustic propagation, is considered in section 3.3.

3.2 Mutual Coherence Function

The main effect of turbulence on tracking arrays is to reduce the coherence of the signal received between the individual array elements. This effect is normally quantified by the transverse *mutual coherence function* (MCF). If $p_m(t)$ and $p_n(t)$ are the signals at two sensors whose separation ρ is parallel to the wavefronts (transverse to the propagation direction), the MCF is defined as

$$\Gamma(\rho) = \frac{\langle p_m(t)p_n^*(t) \rangle}{\langle p_m(t)p_m^*(t) \rangle}.$$

(It is assumed that the average mean intensity at the two receivers matches, i.e., $\langle p_m(t)p_m^*(t) \rangle = \langle p_n(t)p_n^*(t) \rangle$.)

Assuming the turbulence is homogeneous and isotropic, the MCF is given by (Tatarskii, 1971)

$$\Gamma(\rho) = \exp \left\{ -\frac{\pi k^2 x}{2} [b_{eff}(0) - b_{eff}(\rho)] \right\}, \quad (3.4)$$

where x is the propagation distance, $\rho^2 = (y_m - y_n)^2 + (z_m - z_n)^2$, and $b_{eff}(\rho)$ is called the *effective two-dimensional correlation function* (TCF).^{*†} The TCF is a special type of correlation function involving the effective index of refraction. (See the definition and note on terminology in the appendix.) It has two terms, one of which results from the actual fluctuations in the index of refraction, and the second from velocity fluctuations (Ostashev, 1994):

$$b_{eff}(\rho) = b(\rho) + b_{11}(\rho). \quad (3.5)$$

3.3 Turbulence Models

The problem of modeling the turbulence effect on the sensors has now been reduced to one of modeling the TCFs of the turbulence field, $b(\rho)$ and $b_{11}(\rho)$. The appendix shows how equations for the TCFs can be developed for two particular turbulence models, the Gaussian and von Kármán. Both the Gaussian and von Kármán models come in two forms, one for scalars (e.g., the

^{*}Instead of equation (3.4), the formula for the MCF is often given as (Rytov, Kravtsov and Tatarskii, 1989)

$$\Gamma(\rho) = \exp \left\{ -\pi^2 k^2 x \int_0^\infty [1 - J_0(\kappa_\perp \rho)] \Phi(0, \kappa_2, \kappa_3) \kappa_\perp d\kappa_\perp \right\},$$

where J_0 is the Bessel function of the first kind, and $\kappa_\perp^2 = \kappa_2^2 + \kappa_3^2$. Using the identity

$$J_0(z) = \frac{1}{2\pi} \int_0^{2\pi} \exp(iz \cos \theta) d\theta,$$

and the definition for the TCF (see appendix, eq (A-4)), we can show the two formulas to be equivalent.

[†]Since the array configurations in this text are all horizontal, we could set $z_m = z_n$ and $\rho = y_m - y_n$ at this point. It is better not to do so, however. The main reason is that the turbulence modeling (see the appendix) *must* be done in three dimensions in order to be valid; furthermore, the results in this section are not simplified when written in two-dimensional form.

actual index of refraction), and one for vectors (e.g., the velocity fluctuations). Each form contains two parameters, a variance and a length scale.

The variance parameter for the scalar forms, in either the Gaussian or von Kármán models, is seen from equation (3.2) to be

$$\sigma^2 = \langle \epsilon^2 \rangle = \frac{4 \langle c'^2 \rangle}{c_0^2}. \quad (3.6)$$

For the vector case, we have directly from equation (3.1)

$$\sigma^2 = \frac{4 \langle u_1^2 \rangle}{c_0^2}. \quad (3.7)$$

The length scale parameters used in the Gaussian and von Kármán models are not equivalent. Therefore, a common standard for length scales is needed for comparing the models. The standard I adopt is the so-called *integral length scale*, which, as discussed in the appendix, we can find by integrating the standard correlation function from 0 to ∞ , and then dividing by the variance. For scalar fields, this procedure yields a single integral length scale \mathcal{L} . Two scales can be defined, however, for vector fields: one for which the direction of integration is parallel to the orientation of the velocity components, and one in which the integration is perpendicular to the velocity components. I call these two cases the *parallel* and *perpendicular integral length scales*, denoted by \mathcal{L}_{\parallel} and \mathcal{L}_{\perp} , respectively. In a homogeneous, isotropic turbulent field, $\mathcal{L}_{\parallel} = 2\mathcal{L}_{\perp}$ (Batchelor, 1953).

For the scalar form of the Gaussian model, the equation for the TCF, derived in the appendix, is

$$b(\rho) = \frac{\sigma^2 L}{2\sqrt{\pi}} \exp\left(-\frac{\rho^2}{L^2}\right), \quad (3.8)$$

with the length scale parameter given by

$$L = \frac{2}{\sqrt{\pi}} \mathcal{L}. \quad (3.9)$$

For the vector form of the Gaussian model, the TCF is (see appendix)

$$b_{11}(\rho) = \frac{3\sigma^2 L}{4\sqrt{\pi}} \exp\left(-\frac{\rho^2}{L^2}\right), \quad (3.10)$$

with

$$L = \frac{4}{3\sqrt{\pi}} \mathcal{L}_{\parallel} = \frac{8}{3\sqrt{\pi}} \mathcal{L}_{\perp}. \quad (3.11)$$

The main advantage of the Gaussian model is its analytical convenience. Unfortunately, it is rather unrealistic, because most of its energy occurs concentrated at the scale L . In actuality, turbulent energy spans a broad range of spatial scales. The von Kármán model captures this characteristic of the turbulence much more satisfactorily. In particular, the von Kármán model

includes a realistic inertial subrange, in which the energy decays according to Kolmogorov's $-5/3$ power law (1941). For the scalar form of the von Kármán model, the equation for the TCF, derived in the appendix, is

$$b(\rho) = \frac{2^{7/6}\sigma^2\ell}{3\sqrt{\pi}\Gamma(\nu)} \left(\frac{\rho}{\ell}\right)^{5/6} \left[K_{5/6}\left(\frac{\rho}{\ell}\right) - \frac{\rho}{\ell} K_{1/6}\left(\frac{\rho}{\ell}\right) \right], \quad (3.12)$$

where K_ν is the modified Bessel function of the second kind, and the length scale parameter is

$$\ell = \frac{3\Gamma(\nu)}{2\sqrt{\pi}\Gamma(\nu + 1/2)} \mathcal{L}. \quad (3.13)$$

The result for vectors is

$$b(\rho) = \frac{2^{1/6}\sigma^2\ell}{\sqrt{\pi}\Gamma(\nu)} \left(\frac{\rho}{\ell}\right)^{5/6} \left[K_{5/6}\left(\frac{\rho}{\ell}\right) - \frac{\rho}{\ell} K_{1/6}\left(\frac{\rho}{\ell}\right) \right], \quad (3.14)$$

where

$$\ell = \frac{\Gamma(\nu)}{\sqrt{\pi}\Gamma(\nu + 1/2)} \mathcal{L}_\parallel = \frac{2\Gamma(\nu)}{\sqrt{\pi}\Gamma(\nu + 1/2)} \mathcal{L}_\perp. \quad (3.15)$$

TCFs for the two turbulence models are compared in figure 6. The resulting MCFs are shown in figure 7. One notable feature of the curves is that the Gaussian and von Kármán models are fairly similar. The Gaussian curves for the MCF decay somewhat more quickly, because that model has less small-scale turbulent kinetic energy than the von Kármán model. The fact that the two models yield similar results for the TCF and MCF, despite the more realistic description of the inertial subrange turbulence intrinsic to the von Kármán model, indicates that the inertial subrange turbulence is of secondary importance in this particular application. Although Gaussian models often do not work well in wave propagation applications, in this particular application their usage may be justifiable. I consider this matter again in section 4.1.

Figure 8 shows the MCF for several values of $k^2 x \mathcal{L}$: 1, 10, and 100. This plot makes it clear that signal coherence is reduced dramatically with increasing range and decreasing wavelength.

3.4 Modification of Signal Correlation Matrix

The MCF describes the coherence between two sensors when the incident wavefronts are parallel to the sensor axis. Unfortunately, there is no similar result available for arbitrary orientation between the wavefronts and sensors. I assume here that the coherence between a pair of sensors in such cases can be estimated by multiplication of the phase delay, which would occur in the absence of turbulence by the MCF for parallel incidence. Hence we can include the turbulence effect by setting

$$\mathbf{R}_{ss}(\psi) = \mathbf{S}(\psi) \odot \mathbf{T},$$

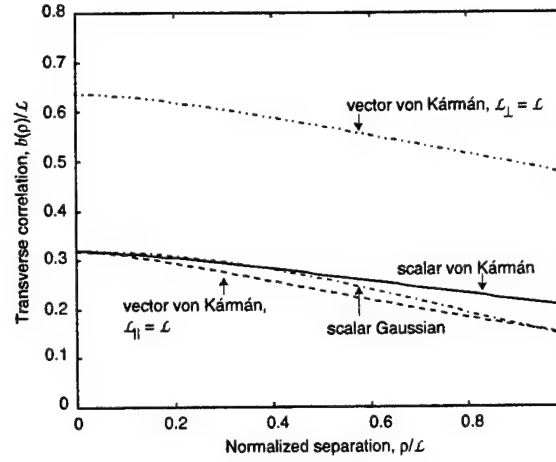


Figure 6: Comparison of transverse correlation functions for different turbulence models.

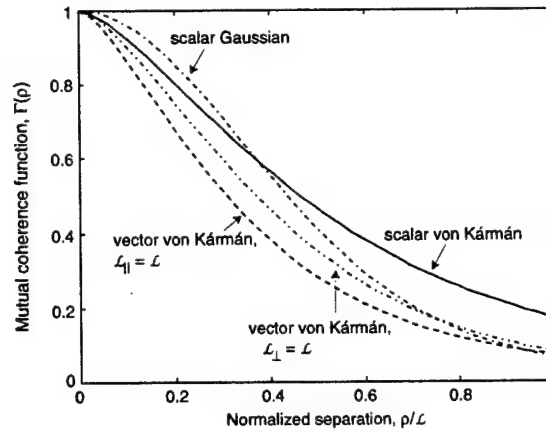


Figure 7: Comparison of mutual coherence functions for several different turbulence models. Value used for $k^2 x \mathcal{L}$ was 10.

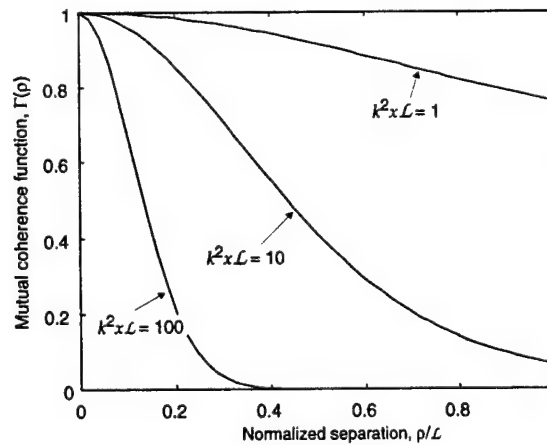


Figure 8: Mutual coherence function for several values of $k^2 x \mathcal{L}$. Scalar form of Gaussian spectrum was used.

where $\mathbf{S}(\psi)$ is the steering matrix (eq (2.6)),

$$T_{mn} = \Gamma(d_{mn}),$$

and the symbol \odot indicates the Hadamard matrix product (simple element-by-element multiplication).

4. Example Calculations and Discussion

4.1 Long Baseline—Sensor Decorrelation Trade-Off

If it were not for cost considerations and turbulence effects, it would be desirable to make acoustic tracking arrays as large as possible. This is evident, for example, from the equation for the CRLB of a two-element array (eq (2.13)). The CRLB in this case is inversely proportional to the square of the sensor spacing. Increasing the array dimensions is desirable because it increases the phase differences between the sensors, making the measurement less sensitive to noise.

On the other hand, large arrays are undesirable when turbulence is considered. Generally, one wants the dimensions of the array small compared to the size of the most energetic turbulent eddies, so that there is good mutual coherence across the array.

The trade-off between array baseline and turbulence degradation is illustrated by the CRLB calculations shown in figure 9. The calculations are for parallel incidence ($\psi = 0$) on a five-element line array, at a normalized distance $kx = 1000$ from the source. The spacing $kd (= 2\pi d/\lambda)$ and strength of the turbulence σ^2 are varied in the figures. The normalized integral length scale is $k\mathcal{L} = 10\pi$, and the noise-to-signal variance is $\sigma_n^2 = 0.1$ (SNR = 10). A scalar von Kármán turbulence spectrum was used.

For weak turbulence ($\sigma^2 \lesssim 10^{-5}$), array performance essentially can be improved without bound by an increase in the sensor spacing. Performance is poor for small sensor spacings, because phase difference information becomes lost in the measurement noise. For strong turbulence ($\sigma^2 \gtrsim 10^{-4}$), array performance is degraded, particularly if the size of the array is comparable to the integral length scale of the turbulence. When this occurs, an “error resonance” in the CRLB is evident. If array dimensions are either much smaller or much larger than the turbulence length scale, however, array performance suffers little.

Figure 10 is similar to 9, except that the noise variance has been decreased to $\sigma_n^2 = 0.01$. Because there is less noise than in the previous example, smaller arrays provide better performance. Although the error resonance for poor array performance is still clearly evident on the figure, now some turbulent degradation of array performance is observed, even for the smaller arrays.

A scalar Gaussian spectrum for $\sigma_n^2 = 0.01$ is shown in figure 11. The error resonance in strong turbulence is sharper in the Gaussian spectrum, while the error for small arrays ($2d/\lambda < 1$) is somewhat less. This difference results from a deficiency of the Gaussian model, discussed earlier: this model does not realistically capture the energy in the small-scale turbulence.

4.2 Dependence of Array Performance on Meteorological Conditions

In order to estimate lower bounds on array performance for actual scenarios, we need values of the turbulence spectral parameters σ^2 and \mathcal{L} . Obtaining these is actually quite a challenging problem, since these parameters depend

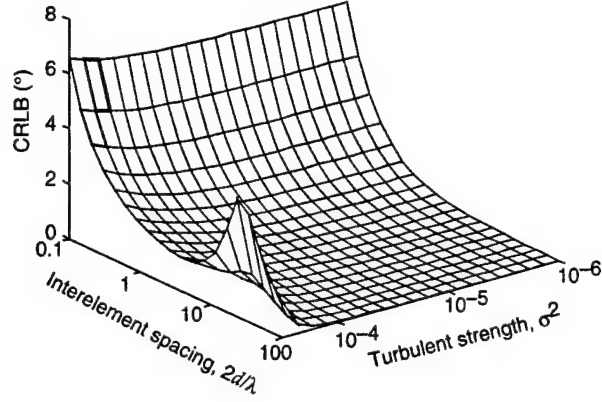


Figure 9: Effect of changing sensor spacing on AOA estimation errors: moderate noise, von Kármán turbulence model case. Array is five-element line array, and calculations are for $\sigma_n^2 = 0.1$, $k\mathcal{L} = 10\pi$.

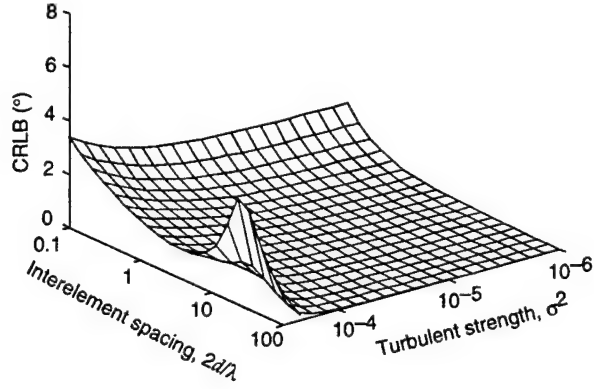


Figure 10: Effect of changing sensor spacing on AOA estimation errors: low-noise, von Kármán turbulence model. Same as figure 9, except that noise variance has been reduced to $\sigma_n^2 = 0.01$.

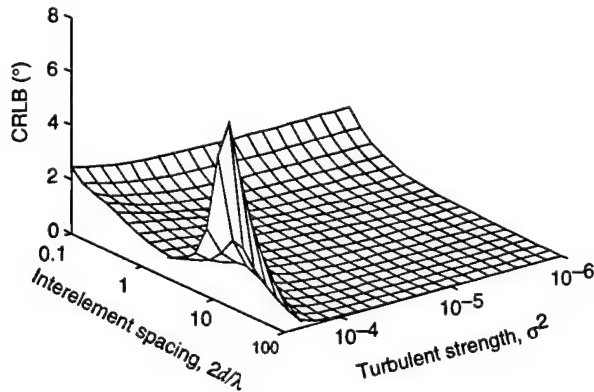


Figure 11: Effect of changing sensor spacing on AOA estimation errors: low-noise, Gaussian turbulence model. Except for change in turbulence model, this is same as figure 10.

strongly on meteorological and topographical conditions. There is no entirely satisfactory turbulence model available. Wilson and Thomson (1994) have proposed a Gaussian turbulence model for acoustical applications that accounts for many of the important features of the turbulence, although, like other Gaussian models, it is unrealistic for the small-scale turbulence structure. Since no comparable von Kármán model is available, I adopt the Wilson and Thomson model for the remaining calculations in this report.

Because the full Wilson and Thomson model is rather complicated, I provide here only a simplified version. The model has three independent physical parameters:

1. The surface wind stress τ . The wind stress increases with increasing wind speed.
2. The surface temperature flux Q , from the ground to the air. The temperature flux is large when the ground is warmer than the overlying air, such as typically occurs when the sun heats the ground.
3. The boundary-layer inversion height z_i . This is the height where the transition occurs between the relatively cool, atmospheric boundary layer air, and warmer air aloft (the free troposphere). In fair weather conditions, this boundary is quite frequently marked by stratocumulus (puffy, flattened) clouds at several hundred to several thousand meters altitude.

It is convenient to define several scaling parameters in terms of the physical ones, τ , Q , and z_i . The *friction velocity* is defined as

$$u_* = \sqrt{\frac{\tau}{\rho}}, \quad (4.1)$$

where ρ is the air density. The *surface-layer temperature scale* is

$$T_* = -\frac{Q}{u_*}. \quad (4.2)$$

The *free-convection velocity scale* is

$$w_* = (Qgz_i/T_s)^{1/3} = (-u_*T_*gz_i/T_s)^{1/3}, \quad (4.3)$$

where g is gravitational acceleration and T_s the surface temperature.

The Wilson and Thomson model includes four additive contributions: small-scale temperature fluctuations, small-scale velocity fluctuations, temperature/velocity covariance, and large-scale velocity fluctuations. The covariance term is neglected in this report. The small-scale temperature (scalar) variance is modeled as

$$\sigma^2 = 4.0 \left(\frac{T_*}{T_s} \right)^2.$$

The small-scale velocity (vector) variance is

$$\sigma^2 = 20 \left(\frac{u_*}{c_0} \right)^2.$$

For both of the small-scale contributions, the corresponding length scales simply equal the height:

$$L = z.$$

The large-scale velocity (vector) variance is

$$\sigma^2 = 0.80 \left(\frac{w_*}{c_0} \right)^2,$$

with corresponding length scale

$$L = 0.4z_i.$$

From equation (3.8), the resulting scalar TCF is

$$b(\rho) = 1.1z \left(\frac{T_*}{T_s} \right)^2 \exp \left(-\frac{\rho^2}{z^2} \right), \quad (4.4)$$

while from equation (3.10) the vector TCF is

$$b_{11}(\rho) = 8.4z \left(\frac{u_*}{c_0} \right)^2 \exp \left(-\frac{\rho^2}{z^2} \right) + 0.14z_i \left(\frac{w_*}{c_0} \right)^2 \exp \left(-\frac{\rho^2}{0.16z_i^2} \right). \quad (4.5)$$

The effective TCF is simply the sum of $b(\rho)$ and $b_{11}(\rho)$ (see eq (3.5)). It is plotted in figure 12 for $u_* = 0.5$ m/s, $T_* = -0.3$ K, $z = 2$ m, and $z_i = 1000$ m. These parameters are representative of a very sunny, somewhat windy afternoon, what atmospheric scientists would call a *convective boundary layer*.

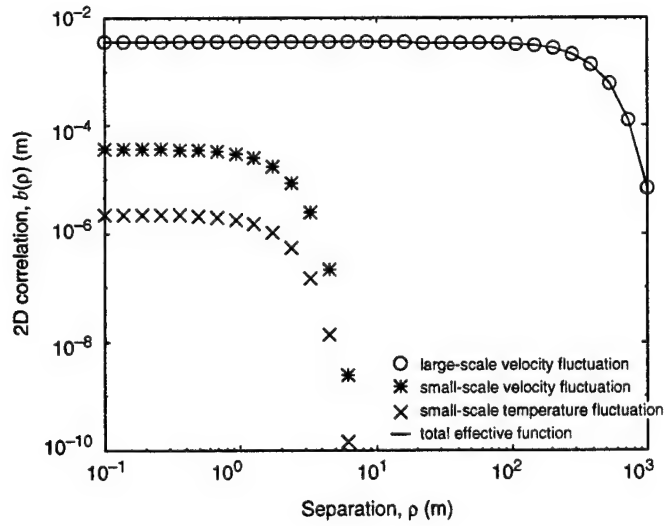


Figure 12: Two-dimensional correlation function (TCF) for convective, atmospheric boundary layer conditions ($u_* = 0.5$ m/s, $T_* = -0.3$ K, $z = 2$ m, and $z_i = 1000$ m).

The figure clearly shows that the large-scale velocity fluctuations (the second term in eq (4.5)) dominate the effective TCF. The reason the TCF is dominated by large-scale structure is evident from the TCF definition (eq (A-4)): by setting $\kappa_1 = 0$ before performing the two-dimensional (2D) inverse Fourier transform, we filter out the small-scale structure.

The observation that large-scale structure dominates the TCF can lead to the incorrect conclusion that large-scale turbulence is most important for determining the MCF. Calculations of the MCF (eq (3.4)) actually depend on the difference $b_{eff}(0) - b_{eff}(\rho)$, not simply $b_{eff}(\rho)$, as was plotted in figure 12. This difference function is plotted for the convective boundary layer case in figure 13. Now we see that, in actuality, the small-scale wind velocity fluctuations are most significant for MCF calculations when $\rho \lesssim 10$ m, the situation of primary interest for acoustical arrays. The large-scale velocity fluctuations become most important only when $\rho \gtrsim 100$ m. Temperature fluctuations are unimportant compared to velocity at all separations.

The difference $b_{eff}(0) - b_{eff}(\rho)$ is plotted for two other cases in figures 14 and 15. Figure 14 is for $u_* = 0.5$ m/s and $T_* = -0.01$ K, with z and z_i the same as earlier. These parameters are representative of what atmospheric scientists call *neutral* conditions, such as normally occur on an overcast, windy day. Figure 15 is for $u_* = 0.1$ m/s and $T_* = 0.01$ K, representative of calm conditions. In these two cases, as before, small-scale velocity fluctuations are dominant when $\rho \lesssim 10$.

Example calculations of the MCF as a function of u_* and T_* are shown in figure 16. The calculations are for ρ equal to one-half wavelength, $f = 200$ Hz, $z = 2$ m, $z_i = 1000$ m, and propagation distance $x = 500$ m. The resulting CRLB is shown in figure 17 for a five-element line array, with spacing $\lambda/2$, at parallel incidence ($\psi = 0$). The number of samples was chosen as $M = 5$, and the noise variance was low, $\sigma_n^2 = 0.01$ (SNR = 20).

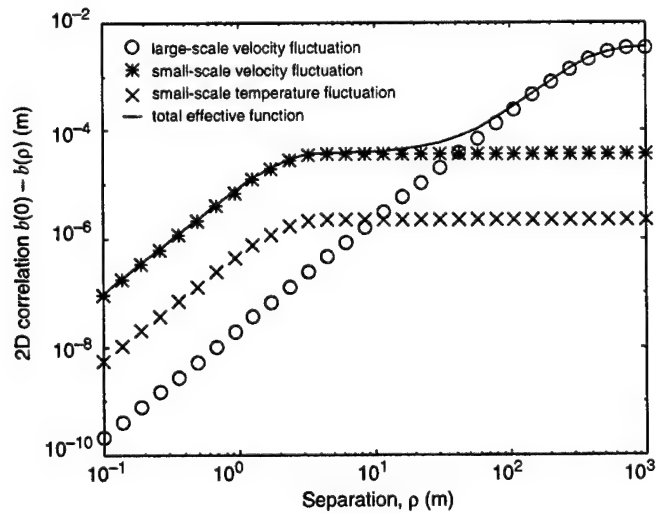


Figure 13: TCF difference function $b_{eff}(0) - b_{eff}(\rho)$ for convective boundary layer conditions.

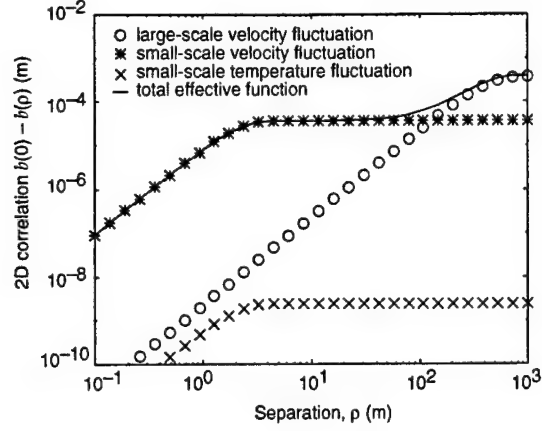


Figure 14: TCF difference function $b_{eff}(0) - b_{eff}(\rho)$ for nearly neutral conditions: $u_* = 0.5$ m/s, $T_* = -0.01$ K, $z = 2$ m, and $z_i = 1000$ m.

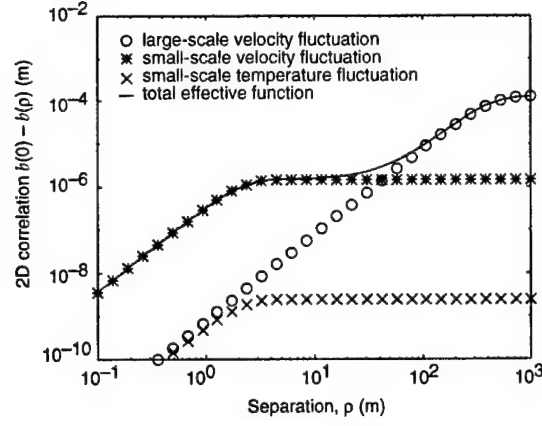


Figure 15: TCF difference function $b_{eff}(0) - b_{eff}(\rho)$ for calm boundary layer conditions: $u_* = 0.1$ m/s, $T_* = 0.01$ K, $z = 2$ m, and $z_i = 1000$ m.

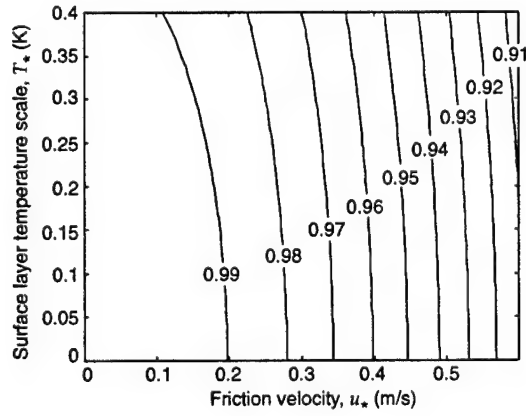


Figure 16: MCF calculations as a function of turbulence conditions. Propagation distance 500 m, frequency 200 Hz, and spacing one-half wavelength.

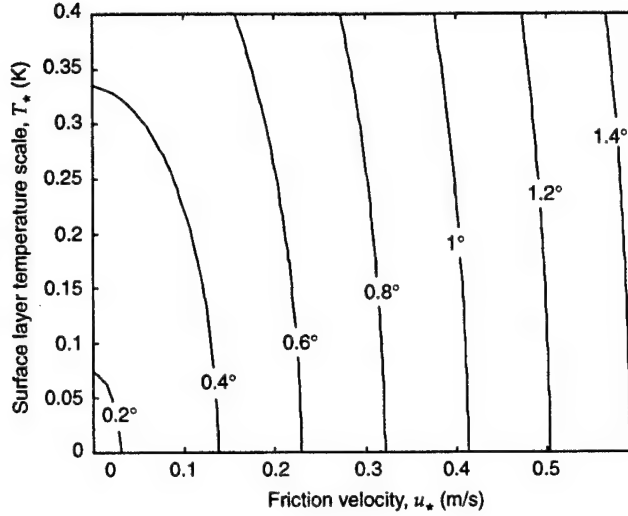


Figure 17: CRLB as a function of turbulence conditions, for a five-element line array at parallel incidence. Propagation distance 500 m, frequency 200 Hz, and sensor spacing one-half wavelength.

4.3 Calculations for Circular RNADS Array

The purpose of ARL's RNADS is to acoustically detect ground and air targets in battlefield environments (Srouf and Robertson, 1995). The normal configuration for the acoustic array, shown in figure 18, has seven sensors: six spaced equally along a circle, and a seventh at the origin. In this section, I examine the theoretically best obtainable performance (CRLB) by the RNADS array in various turbulent environments. CRLB calculations are provided for the same three representative cases of turbulence parameters discussed in section 4.2: convective ($u_* = 0.5$ m/s, $T_* = -0.3$ K), neutral ($u_* = 0.5$ m/s, $T_* = -0.01$ K), and calm ($u_* = 0.1$ m/s, $T_* = -0.01$ K). In all cases I set $z = 2$ m, $z_i = 1000$ m, and $M = 5$. Note, as discussed in section 2, that regular polygons such as the RNADS array have a CRLB that is independent of the AOA ψ . Therefore, it is unnecessary to plot the CRLB as a function of ψ for RNADS.

Two sets of calculations for convective conditions are shown in figures 19 and 20, as a function of the propagation distance and the acoustic frequency. The difference between the figures is the value used for the noise variance: $\sigma_n^2 = 0.01$ (SNR = 20 dB) for figure 19, and $\sigma_n^2 = 1$ (SNR = 0 dB) for figure 20. For both noise scenarios, there is an increase in AOA fidelity (decrease in the CRLB) with increasing frequency. This is because the wavelength decreases with increasing frequency, thereby increasing the dimensions of the array relative to a wavelength. (Recall from sect. 4.1 that large arrays, relative to the wavelength, have greater phase differences between the elements, so that noise is mitigated.) In the low SNR case, the CRLB is much higher, particularly for short propagation distances. In fact, the CRLB is nearly independent of propagation distance for low SNR. This is characteristic of a *noise-limited array*, meaning that noise is the dominant factor determin-

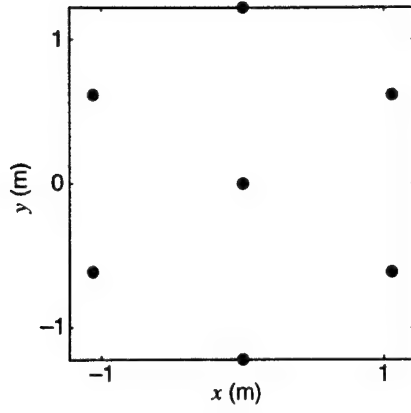


Figure 18: Sensor layout for circular RNADS array in a horizontal plane. Sensors are shown as dark circles.

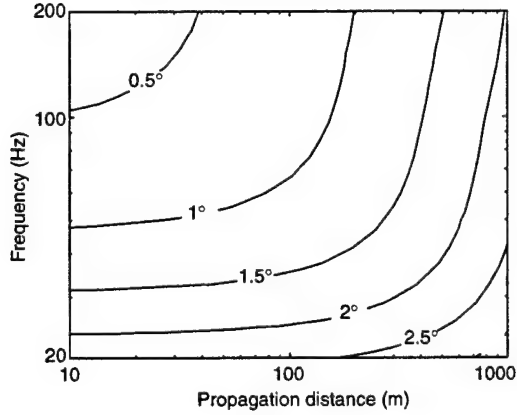


Figure 19: CRLB for circular RNADS array in convective atmospheric boundary layer, low-noise case. SNR is 20 dB.

ing array performance. For high SNR, the array is noise limited for short propagation distances, after which the CRLB rapidly increases. This rapid increase marks the distance where the array becomes *turbulence limited*. The transition distance becomes shorter as the frequency is increased.

The near-neutral atmospheric case, with $\sigma_n^2 = 0.01$, is shown in figure 21. This case looks nearly identical to the convective, high-SNR case (fig. 19). The reason for this similarity is that the values used for u_* in the convective and neutral cases were the same, and the CRLB responds primarily to small-scale velocity fluctuations (the u_* term in eq (4.5)).

The calm atmospheric case, with $\sigma_n^2 = 0.01$, is shown in figure 22. Although the SNR is high in this case, it looks qualitatively similar to the low-SNR convective case (fig. 20). This is because both cases are essentially noise limited. The turbulence in the calm atmosphere is not strong enough to affect the CRLB, at least for the range of frequencies and propagation distances shown.

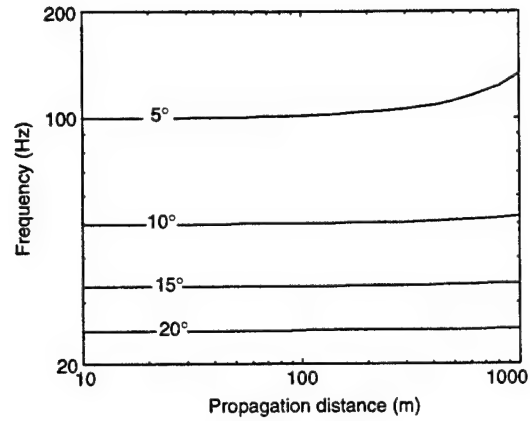


Figure 20: CRLB for circular RNADS array in convective atmospheric boundary layer, high-noise case. SNR is 0 dB.

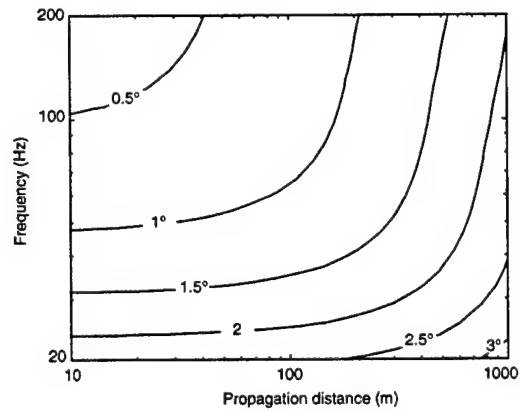


Figure 21: CRLB for circular RNADS array in neutral atmospheric boundary layer, low-noise case. SNR is 20 dB.

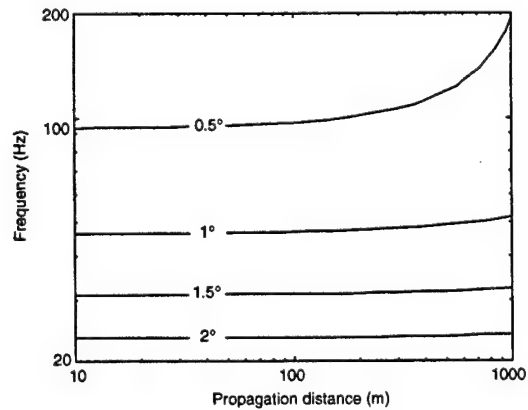


Figure 22: CRLB for circular RNADS array in calm atmospheric boundary layer, low-noise case. SNR is 20 dB.

5. Conclusions

Turbulence limits our ability to obtain accurate AOA estimates using acoustic sensor arrays, particularly in low-noise environments. Fortunately, the calculations in this paper suggest that the AOA can be measured to an accuracy of several degrees or better, even in strong turbulence, by the use of an array with just a half dozen or so sensors.

Turbulence effects on acoustic sensor arrays are most significant under the following conditions:

- Sufficiently energetic turbulence is present. The type of turbulence that predominantly affects acoustic arrays is small-scale turbulence generated by near-ground wind shear instabilities, the strength of which is parameterized by the friction velocity u_* .
- There is low background noise, so that array performance is limited by turbulence, rather than noise.
- Array dimensions are comparable in size to the most energetic turbulent eddies. This is usually true for the arrays of interest in current Army applications.

Examples given in this report demonstrate that the turbulence model used to calculate array performance assessments can dramatically affect the results. In particular, a von Kármán turbulence spectrum is generally preferable to a Gaussian spectrum, since it models inertial subrange turbulence more realistically.

6. Recommendations

In this report, I have only scratched the surface of the many signal processing, turbulence modeling, and acoustic propagation issues relevant to design and performance assessment of acoustical tracking arrays. There are numerous areas for future research that will help improve our understanding and enhance the performance of acoustical systems:

1. Most importantly, the theory and predictions developed in this report should be tested by a comparison to field data.
2. The propagating wavefronts were assumed to be planar in this report. It would be very desirable to extend the theory to include spherical wavefronts, since in many situations of practical importance the sensor array will be close to the source.
3. The assumption of uncorrelated noise at the sensor, as made in section 2.2, is very unrealistic. The potential importance of using realistic noise models needs to be explored.
4. Acoustic tracking demonstrations previously performed by ARL (Srouer and Robertson, 1995) have often used several separate independent arrays, each similar to the one shown in figure 18. The main reason for deploying multiple arrays in this fashion is to allow determination of the actual location (not just the AOA) of the acoustic source. It would, of course, be desirable to calculate performance estimates for these multiple-array deployments. Performance assessments also are needed when there are multiple sources.
5. Improved turbulence models, including realistic inhomogeneity and anisotropy characteristic of atmospheric turbulence (Mann, 1994; Wilson, 1996b), should be considered in future research.
6. In field studies, acoustic tracking has sometimes been found to undergo periods of intermittent target loss (Pham and Sadler, 1995). The likely cause of such dropouts is a failure of the tracking algorithm brought about by an intermittent change in the meteorological conditions. Previously (Wilson, (1996a)), I considered the effect of turbulent intermittency on acoustic detection in shadows. Future research should extend that work to acoustical tracking scenarios.

Appendix A. Statistical Turbulence Models

In order to determine the mutual coherence function (MCF), and hence model the turbulence effect on a sensor array, we need a spectral model for the turbulence field. The mathematics involved in properly defining and manipulating turbulence spectra is rather complicated. The relevant equations are summarized in this appendix and applied to two different turbulence models: the Gaussian and von Kármán.

A-1. Correlation and Spectral Functions

Let us define the correlation function of a scalar quantity c as

$$R(r_1, r_2, r_3) = \langle c(x'_1, x'_2, x'_3) c(x_1, x_2, x_3) \rangle, \quad (\text{A-1})$$

where $r_1 = x'_1 - x_1$, etc. For this definition, it has been assumed that the field is *homogeneous*: its statistics depend only on the displacement between the measurement points. If the field is also *isotropic* (i.e., its statistics are independent of coordinate rotations), then the correlation function for a scalar actually depends only on the radial distance r between the measurement points, where $r^2 = r_1^2 + r_2^2 + r_3^2$. In this case, we can write $R(r) = R(r_1, r_2, r_3)$ for short.

The three-dimensional spectral density function (spectrum, for short) is the three-dimensional Fourier transform of the correlation function:

$$\Phi(\kappa_1, \kappa_2, \kappa_3) = \frac{1}{8\pi^3} \int_{-\infty}^{\infty} \int_{-\infty}^{\infty} \int_{-\infty}^{\infty} R(r_1, r_2, r_3) \exp[-i(\kappa_1 r_1 + \kappa_2 r_2 + \kappa_3 r_3)] dr_1 dr_2 dr_3, \quad (\text{A-2})$$

$$R(r_1, r_2, r_3) = \int_{-\infty}^{\infty} \int_{-\infty}^{\infty} \int_{-\infty}^{\infty} \Phi(\kappa_1, \kappa_2, \kappa_3) \exp[i(\kappa_1 r_1 + \kappa_2 r_2 + \kappa_3 r_3)] d\kappa_1 d\kappa_2 d\kappa_3. \quad (\text{A-3})$$

The two-dimensional correlation function (TCF, which is required to compute the MCF in sect. 3.2) is defined as the two-dimensional inverse Fourier transform of $\Phi(0, \kappa_2, \kappa_3)$:

$$b(\rho) = \int_{-\infty}^{\infty} \int_{-\infty}^{\infty} \Phi(0, \kappa_2, \kappa_3) \exp[i(\kappa_2 r_2 + \kappa_3 r_3)] d\kappa_2 d\kappa_3. \quad (\text{A-4})$$

Equivalently, by Fourier transforming (A-3) with respect to r_1 and setting $\kappa_1 = 0$, one has

$$b(\rho) = \frac{1}{2\pi} \int_{-\infty}^{\infty} R(r_1, r_2, r_3) dr_1. \quad (\text{A-5})$$

A note on terminology: Other authors have called the TCF the *transverse* (rather than two-dimensional) correlation function. I prefer *two-dimensional*, since we derive the TCF by setting one of the wavenumbers in $\Phi(\kappa_1, \kappa_2, \kappa_3)$ to zero and then taking the inverse Fourier transform in the remaining two

directions. Hence it is the logical counterpart of the two-dimensional spectrum, which we derive by setting one of the displacements in the correlation function $R(r_1, r_2, r_3)$ to zero, and then taking the forward Fourier transform the remaining two directions.

Vector quantities, such as turbulent velocity fluctuations, are handled similarly. However, the situation becomes somewhat more complicated for vectors, since three directions are definable in a given spectrum or correlation: the direction of the displacement, and also the orientations of the two velocity components under consideration. (Only the direction of the displacement is involved in the scalar case.) Let us define the correlation as

$$R_{ij}(r_1, r_2, r_3) = \langle u_i(x'_1, x'_2, x'_3) u_j(x_1, x_2, x_3) \rangle, \quad (\text{A-6})$$

where the subscripts i and j indicate the velocity component. Note that R_{ij} is a tensor quantity, having nine components. By taking the appropriate Fourier transforms in a manner analogous to the scalar case, we can define tensors for the spectral density and TCF.

A-2. Energy Spectra

If only scalar quantities were of interest, it would be a straightforward matter to propose a model for the correlation function or the three-dimensional spectrum, and then integrate to find the TCF. But in the vector case, since there are nine possible combinations for the values of i and j in the correlation tensor (eq (A-6)), trying to model the correlation functions or spectral density tensors directly can become complicated. It turns out to be somewhat easier to start with a model for a scalar quantity that is a property of both scalar and vector fields, such as energy. For consistency, I adopt this approach in both the scalar and vector cases. The *energy spectrum* $E(\kappa)$ is defined such that its integral over the wavenumber domain equals half the total variance of the field. For a scalar quantity,

$$\int_0^\infty E(\kappa) d\kappa = \frac{\sigma^2}{2}. \quad (\text{A-7})$$

Note from the Fourier transform relation (eq (A-3)), with $r_1 = r_2 = r_3 = 0$,

$$\sigma^2 = \int_{-\infty}^\infty \int_{-\infty}^\infty \int_{-\infty}^\infty \Phi(\kappa_1, \kappa_2, \kappa_3) d\kappa_1 d\kappa_2 d\kappa_3.$$

Hence, we find the three-dimensional spectrum $\Phi(\kappa)$ by multiplying $E(\kappa)$ by two, and then dividing by the “area” of a spherical shell in wavenumber space, $4\pi\kappa^2$:

$$\Phi(\kappa) = \frac{E(\kappa)}{2\pi\kappa^2}. \quad (\text{A-8})$$

Substituting into the definition of the TCF (eq (A-4)), we obtain

$$b(\rho) = \frac{1}{2\pi} \int_{-\infty}^\infty \int_{-\infty}^\infty \frac{E\left(\sqrt{\kappa_2^2 + \kappa_3^2}\right)}{\kappa_2^2 + \kappa_3^2} \exp[i(\kappa_2 r_2 + \kappa_3 r_3)] d\kappa_2 d\kappa_3, \quad (\text{A-9})$$

where $\rho^2 = r_2^2 + r_3^2$.

For vectors, such as the turbulent velocities, $E(\kappa)$ is defined such that

$$\int_0^\infty E(\kappa) d\kappa = \frac{3\sigma^2}{2}. \quad (\text{A-10})$$

If this definition is used, σ^2 represents the variance in just one of the three velocity components. The three-dimensional spectra are related to the energy spectrum according to (Batchelor, 1953)

$$\Phi_{ij}(\kappa) = \frac{E(\kappa)}{4\pi\kappa^4} (\delta_{ij}\kappa^2 - \kappa_i\kappa_j). \quad (\text{A-11})$$

From the above, the reader can verify, analogously to the scalar case, that

$$\Phi_{11}(\kappa) + \Phi_{22}(\kappa) + \Phi_{33}(\kappa) = \frac{E(\kappa)}{2\pi\kappa^2}.$$

Substituting $\Phi_{11}(\kappa)$, as given by equation (A-11), into the definition of the TCF (eq (A-4)), we have

$$b_{11}(\rho) = \frac{1}{4\pi} \int_{-\infty}^{\infty} \int_{-\infty}^{\infty} \frac{E(\sqrt{\kappa_2^2 + \kappa_3^2})}{\kappa_2^2 + \kappa_3^2} \exp[i(\kappa_2 r_2 + \kappa_3 r_3)] d\kappa_2 d\kappa_3. \quad (\text{A-12})$$

Quite interestingly, this result is exactly half the result for a scalar. Hence, if we choose the same functional form for the energy spectrum in both the scalar and vector cases, the resulting TCFs will likewise have the same functional form.

A-3. Length Scales

It is important that we be able to accurately quantify length scales associated with given spectra. By *length scale*, I mean a value representative of the size of the most energetic eddies in the spectrum. For a scalar quantity, the *integral length scale* is defined as

$$\mathcal{L} = \frac{1}{\sigma^2} \int_0^\infty R(r) dr. \quad (\text{A-13})$$

It turns out that the integral length scale and TCF are simply related. From the Fourier transform relation between the correlation function and the spectrum, and from equation (A-8), we have

$$\frac{1}{2\pi} \int_{-\infty}^{\infty} R(r_1, 0, 0) e^{-i\kappa_1 r_1} dr_1 = \int_{-\infty}^{\infty} \int_{-\infty}^{\infty} \frac{E(\kappa)}{2\pi\kappa^2} e^{i(\kappa_2 r_2 + \kappa_3 r_3)} d\kappa_2 d\kappa_3.$$

Setting $r_2 = r_3 = 0$, $\kappa_1 = 0$, and using the fact that $R(r_1, 0, 0)$ is an even function, we obtain

$$\frac{1}{\pi} \int_0^\infty R(r_1, 0, 0) dr_1 = \frac{1}{2\pi} \int_{-\infty}^{\infty} \int_{-\infty}^{\infty} \frac{E(\sqrt{\kappa_2^2 + \kappa_3^2})}{\kappa_2^2 + \kappa_3^2} d\kappa_2 d\kappa_3.$$

Comparing now with equation (A-9), we find that

$$\mathcal{L} = \frac{\pi}{\sigma^2} b(0). \quad (\text{A-14})$$

In the vector case, the direction of the velocity components as well as the direction of the displacement must be considered. Two significant scales can be defined: one where the displacement is parallel to the velocity, e.g.,

$$\mathcal{L}_{\parallel} = \frac{1}{\sigma^2} \int_0^{\infty} R_{11}(r_1, 0, 0) dr_1,$$

and the other where it is perpendicular, e.g.,

$$\mathcal{L}_{\perp} = \frac{1}{\sigma^2} \int_0^{\infty} R_{22}(r_1, 0, 0) dr_1.$$

For homogeneous, isotropic turbulence, it can be proven that (Batchelor, 1953)

$$\mathcal{L}_{\parallel} = 2\mathcal{L}_{\perp}. \quad (\text{A-15})$$

Furthermore, using a derivation similar to the scalar case, one finds

$$\mathcal{L}_{\parallel} = \frac{\pi}{\sigma^2} b_{11}(0). \quad (\text{A-16})$$

A-4. Gaussian Model

Let us now consider specific models for atmospheric turbulence. Unfortunately, we do not now have (and probably never will have) three-dimensional turbulence models that are known to work satisfactorily for a variety of atmospheric conditions. Hence, we are forced to consider idealized models. In this section, I describe one such idealization, the Gaussian model. The main advantage of the Gaussian model is its analytical convenience; unfortunately, it can work well for qualitatively modeling only the largest scale features of the turbulence (called the *energy-containing subrange*). The von Kármán model, described in section A-5, is somewhat more general, since it also describes well the smaller scale eddies (the *inertial subrange*).

It is customary to define the Gaussian model in terms of its three-dimensional correlation function $R(r)$. For the scalar case,

$$R(r) = \sigma^2 \exp\left(-\frac{r^2}{L^2}\right), \quad (\text{A-17})$$

where L is a length scale. The corresponding three-dimensional spectrum, found by Fourier transformation of the correlation function in all three dimensions, is

$$\Phi(\kappa) = \frac{\sigma^2 L^3}{8\pi^{3/2}} \exp\left(-\frac{\kappa^2 L^2}{4}\right). \quad (\text{A-18})$$

The energy spectrum, which follows from multiplication by $2\pi\kappa^2$, is shown in figure A-1.

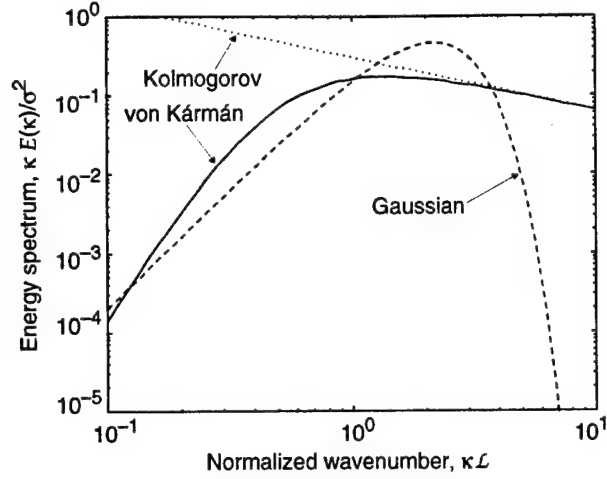


Figure A-1: Comparison of Gaussian and von Kármán energy spectral models.

The TCF is found from the energy spectrum and equation (A-9). The integration is not difficult for the Gaussian function, with the result being

$$b(\rho) = \frac{\sigma^2 L}{2\sqrt{\pi}} \exp\left(-\frac{\rho^2}{L^2}\right). \quad (\text{A-19})$$

Hence from equation (A-14), we have

$$\mathcal{L} = \frac{\sqrt{\pi}}{2} L. \quad (\text{A-20})$$

We find the TCF for the velocity field by multiplying by 3 (to account for the vector nature of this quantity, see eq (A-10)), and then dividing by 2, as discussed earlier in connection with equation (A-12). By equation (A-16), then,

$$\mathcal{L}_{\parallel} = \frac{3\sqrt{\pi}}{4} L. \quad (\text{A-21})$$

A-5. Von Kármán Model

The von Kármán type of model is developed directly from the following proposed form for the energy spectrum of a scalar:

$$E(\kappa) = \frac{4\Gamma(\nu + 5/2)}{3\sqrt{\pi}\Gamma(\nu)} \frac{\sigma^2 \kappa^4 \ell^5}{(1 + \kappa^2 \ell^2)^{\nu+5/2}}. \quad (\text{A-22})$$

The parameter ℓ is a characteristic length scale, and ν controls the power-law dependence in the inertial subrange ($\kappa\ell \gg 1$). Generally, we set $\nu = 1/3$ to obtain Kolmogorov's $\kappa^{-5/3}$ power law for the inertial subrange. The von Kármán model is compared to the Gaussian model in figure A-1. The main difference between the von Kármán and Gaussian models is that the Gaussian model decays much more rapidly at large wavenumbers.

Calculating the TCF from relationship (A-9), we find

$$b(\rho) = \frac{2^{3/2-\nu}\sigma^2\ell}{3\sqrt{\pi}\Gamma(\nu)} \left(\frac{\rho}{\ell}\right)^{\nu+1/2} \left[K_{\nu+1/2}\left(\frac{\rho}{\ell}\right) - \frac{\rho}{\ell} K_{\nu-1/2}\left(\frac{\rho}{\ell}\right) \right]. \quad (\text{A-23})$$

Integrals (3.773.6) and (6.726.4) in Gradshteyn and Ryzhik (1994) were used to derive this result. K_ν is the modified Bessel function of the second kind. As discussed above, the result $b_{11}(\rho)$ for vectors is simply 3/2 times the scalar result.

Integral length scales can be derived by replacement of the Bessel functions by the first term in their Taylor series expansions. The result for scalars is

$$\mathcal{L} = \frac{2\sqrt{\pi}\Gamma(\nu+1/2)}{3\Gamma(\nu)}\ell. \quad (\text{A-24})$$

For vectors,

$$\mathcal{L}_{\parallel} = \frac{\sqrt{\pi}\Gamma(\nu+1/2)}{\Gamma(\nu)}\ell. \quad (\text{A-25})$$

From equation (A-20) and (A-24), it can be shown that L for the Gaussian model is 1.78 times ℓ for the von Kármán model, assuming the same value for \mathcal{L} is used in each case.

References

- Batchelor, G. K. (1953): *The Theory of Homogeneous Turbulence*. Cambridge Univ. Press, Cambridge, Great Britain.
- Burdic, W. S. (1984): *Underwater Acoustic Signal Analysis*. Prentice-Hall, Englewood Cliffs, New Jersey.
- Daigle, G. A., J. E. Piercy, and T.F.W. Embleton (1983): Line-of-sight propagation through atmospheric turbulence near the ground. *J. Acoust. Soc. Am.* **74**, 1505-1513.
- Gradshteyn, I. S., and I. M. Ryzhik (1994): *Table of Integrals, Series, and Products*. Academic Press, San Diego.
- Havelock, D. I., X. Di, G. A. Daigle, and M. R. Stinson (1995): Spatial coherence of a sound field in a refractive shadow: Comparison of simulation and experiment. *J. Acoust. Soc. Am.* **98**, 2289-2302.
- Kinsler, L. E., A. R. Frey, A. B. Coppens, and J. V. Sanders (1982): *Fundamentals of Acoustics*. Wiley and Sons, New York.
- Kolmogorov, A. N. (1941): The local structure of turbulence in incompressible viscous fluid for very large Reynolds numbers. *C. R. Acad. Sci. URSS* **30**, 301-305.
- Mann, J. (1994): The spatial structure of neutral atmospheric surface layer turbulence. *J. Fluid Mech.* **273**, 141-168.
- Ostashev, V. E. (1994): Sound propagation and scattering in media with random inhomogeneities of sound speed, density and medium velocity. *Waves Rand. Med.* **4**, 403-428.
- Pham, T., and B. M. Sadler (1995): Aeroacoustic wideband array processing for detection and tracking of ground vehicles. *Program of the 130th Meeting*, Acoustical Society of America, St. Louis, Missouri.
- Rytov, S. M., Y. A. Kravtsov, and V. I. Tatarskii (1989): *Principles of Statistical Radio Physics, Part 4: Wave Propagation through Random Media*. Springer, Berlin.
- Scharf, L. L. (1991): *Statistical Signal Processing: Detection, Estimation, and Time Series Analysis*. Addison-Wesley, Reading, Massachusetts.
- Song, B.-G., and J. A. Ritcey (1996): Angle of arrival estimation of plane waves propagating in random media. *J. Acoust. Soc. Am.* **99**, 1370-1379.
- Srour, N., and J. Robertson (1995): *Remote Netted Acoustic Detection System: Final Report*. U.S. Army Research Laboratory, ARL-TR-706.
- Tatarskii, V. I. (1961): *Wave Propagation in a Turbulent Medium*. McGraw-Hill, New York.

- Tatarskii, V. I. (1971): *The Effects of the Turbulent Atmosphere on Wave Propagation*. Keter, Jerusalem.
- Wilson, D. K. (1996): *The Effect of Turbulent Intermittency on Detection in Acoustic Shadows*. U.S. Army Research Laboratory, ARL-TR-1002.
- Wilson, D. K. (1997): *Three-Dimensional Correlation and Spectral Functions for Turbulent Velocities in Homogeneous and Surface-Blocked Boundary Layers*. U.S. Army Research Laboratory, ARL-TR-1287.
- Wilson, D. K., and D. W. Thomson (1994): Acoustic propagation through anisotropic, surface-layer turbulence. *J. Acoust. Soc. Am.* **96**, 1080–1095.

Acronyms

AOA	angle of arrival
AOB	angle of bearing
ARL	Army Research Laboratory
CRLB	Cramer-Rao lower bound (or its square root)
MCF	mutual coherence function
mse	mean square error
TCF	two-dimensional correlation function
RNADS	Remote Netted Acoustic Detection System
SNR	signal-to-noise ratio

Distribution

Admnstr
Defns Techl Info Ctr
Attn DTIC-OCF
8725 John J Kingman Rd Ste 0944
FT Belvoir VA 22060-6218

Mil Asst for Env Sci
Ofc of the Undersec of Defns for Rsrch &
Engrg R&AT E LS
Pentagon Rm 3ED129
Washington DC 20301-3080

Ofc of the Secy of Defs
Attn ODDRE (R&AT) G Singley
Attn ODDRE (R&AT) S Gontarek
The Pentagon
Washington DC 20301-3080

ARL Chemical Biology Nuc Effects Div
Attn AMSRL-SL-CO
Aberdeen Proving Ground MD 21005-5423

Army ARDEC
Attn SMCAR-IMI-I
BLDG 59
Dover NJ 07806-5000

Army Communications Elec Ctr for EW RSTA
Attn AMSEL-EW-D
Attn AMSEL-EW-MD
FT Monmouth NJ 07703-5303

Army Corps of Engrg
Attn ETL-GS-LB
FT Belvoir VA 22060

Army Dugway Proving Ground
Attn STEDP 3
Attn STEDP-MT-DA-L-3
Attn STEDP-MT-M Bowers
Dugway UT 84022-5000

Army Field Artillery School
Attn ATSF-TSM-TA
FT Sill OK 73503-5000

Army Foreign Sci Tech Ctr
Attn CM
220 7th Stret NE
Charlottesville VA 22901-5396

Army Infantry
Attn ATSH-CD-CS-OR E Dutoit
FT Benning GA 30905-5090

Army Materiel Sys Analysis Activity
Attn AMXSY H Cohen
Attn AMXSY-AT Campbell
Attn AMXSY-CR Marchet
Attn AMXSY-CS Bradley
Aberdeen Proving Ground MD 21005-5071

Army Missile Cmnd
Attn AMSMI-RD-CS-R Doc
Redstone Arsenal AL 35898-5241

Army Missile Cmnd
Attn AMSMI-RD-AC-AD Peterson
Redstone Arsenal AL 35898-5242

Army Missile Cmnd
Attn AMSMI-RD-DE-SE G Lill Jr
Redstone Arsenal AL 35898-5245

Army Missile Cmnd
Attn AMSMI-RD-AS-SS H F Anderson
Attn AMSMI-RD-AS-SS B Williams
Redstone Arsenal AL 35898-5253

Army Nuclear Cml Agency
Attn MONA ZB
Bldg 2073
Springfield VA 22150-3198

Army OEC
Attn CSTE EFS
4501 Ford Ave Park Center IV
Alexandria VA 22302-1458

Army Rsrch Ofc
Attn AMXRO-GS Bach
PO Box 12211
Research Triangle Park NC 27709

Army Satellite Comm Agcy
Attn DRCPM SC 3
FT Monmouth NJ 07703-5303

Army Strat Defns Cmnd
Attn CSSD-SL-L Lilly
PO Box 1500
Huntsville AL 35807-3801

Distribution

Army Topo Engr Ctr
Attn CETEC-ZC-1
FT Belvoir VA 22060-5546

CECOM
Attn PM GPS COL S Young
FT Monmouth NJ 07703

CECOM RDEC Electronic Systems Div Dir
Attn J Niemela
FT Monmouth NJ 07703

CECOM
Sp & Terrestrial Commctn Div
Attn AMSEL-RD-ST-MC-M H Soicher
FT Monmouth NJ 07703-5203

DARPA
Attn B Kaspar
Attn J Pennella
Attn L Stotts
3701 N Fairfax Dr
Arlington VA 22203-1714

Dpty Assist Scy for Rsrch & Techl
Attn SARD-TR R Chait Rm 3E476
Attn SARD-TT D Chait
Attn SARD-TT F Milton Rm 3E479
Attn SARD-TT K Kominos
Attn SARD-TT R Reisman
Attn SARD-TT T Killion
The Pentagon
Washington DC 20310-0103

DUSD Space
Attn 1E765 J G McNeff
3900 Defense Pentagon
Washington DC 20301-3900

Hdqtrs Dept of the Army
Attn DAMO-FDQ D Schmidt
400 Army Pentagon
Washington DC 20310-0460

Kwajalein Missile Range
Attn Meteorologist in Charge
PO Box 57
APO San Francisco CA 96555

Logistics Ctr
Attn ATCL-CE
FT Lee VA 23801-6000

Natl Security Agency
Attn W21 Longbothum
9800 Savage Rd
FT George G Meade MD 20755-6000

Naval Air Dev Ctr
Attn Code 5012 A Salik
Warminster PA 18974

OSD
Attn OUSD(A&T)/ODDDR&E(R) J Lupo
The Pentagon
Washington DC 20301-7100

US Army Matl Cmnd
Dpty CG for RDE Hdqtrs
Attn AMCRD BG Beauchamp
5001 Eisenhower Ave
Alexandria VA 22333-0001

US Army Matl Cmnd
Prin Dpty for Acquisition Hdqtrs
Attn AMCDCG-A D Adams
5001 Eisenhower Ave
Alexandria VA 22333-0001

US Army Matl Cmnd
Prin Dpty for Techlgy Hdqtrs
Attn AMCDCG-T M Fisette
5001 Eisenhower Ave
Alexandria VA 22333-0001

US Army TRADOC Anlys Cmnd—WSMR
Attn ATRC-WSS-R
White Sands Missile Range NM 88002

US Military Academy
Dept of Mathematical Sci
Attn MAJ D Engen
West Point NY 10996

USAASA
Attn MOAS-AI W Parron
9325 Gunston Rd Ste N319
FT Belvoir VA 22060-5582

USACRREL
Attn CEREL-GP R Detsch
72 Lyme Rd
Hanover NH 03755-1290

Distribution

USATRADO
Attn ATCD-FA
FT Monroe VA 23651-5170

Nav Air War Cen Wpn Div
Attn CMD 420000D C0245 A Shlanta
1 Admin Cir
China Lake CA 93555-6001

Naval Surface Weapons Ctr
Attn Code G63
Dahlgren VA 22448-5000

AFMC DOW
Wright Patterson AFB OH 45433-5000

Air Weather Service
Attn Tech Lib FL4414 3
Scott AFB IL 62225-5458

Dept of the Air Force
Attn OL A 2D Weather squad Mac
Holloman AFB NM 88330-5000

GPS Joint Prog Ofc Dir
Attn COL J Clay
2435 Vela Way Ste 1613
Los Angeles AFB CA 90245-5500

Hdqtrs AWS DOO 1
Scott AFB IL 62225-5008

Ofc of the Dir Rsrch and Engrg
Attn R Menz
Pentagon Rm 3E1089
Washington DC 20301-3080

Phillips Lab Atmospheric Sci Div
Geophysics Dirctr
Hanscom AFB MA 01731-5000

Phillips Laboratory
Attn PL/LYP Chisholm
Hanscom AFB MA 01731-5000

Special Assist to the Wing Cmndr
Attn 50SW/CCX CAPT P H Bernstein
300 O'Malley Ave Ste 20
Falcon AFB CO 80912-3020

USAF Rome Lab Tech
Attn Corridor W Ste 262 RL SUL
26 Electr Pkwy Bldg 106
Griffiss AFB NY 13441-4514

USAF SMC/CED
Attn DMA/JPO M Ison
2435 Vela Way Ste 1613
Los Angeles AFB CA 90245-5500

USAFETAC DNE
Attn Glauber
Scott AFB IL 62225-5008

Nasa Marshal Space Flt Ctr
Atmospheric Sciences Div
Attn E501 Fichtl
Huntsville AL 35802

Nasa Spct Flt Ctr
Atmospheric Sciences Div
Attn Code ED 41 1
Huntsville AL 35812

ARL Electromag Group
Attn Campus Mail Code F0250 A Tucker
University of TX
Austin TX 78712

Dept of Commerce Ctr
Mountain Administration
Attn Spprt Ctr Library R51
325 S Broadway
Boulder CO 80303

Lockheed Missile & Spc Co
Attn Org 91 01 B 255 K R Hardy
3251 Hanover Stret
Palo Alto CA 94304-1191

Natl Ctr for Atmospheric Research
Attn NCAR Library Serials
PO Box 3000
Boulder CO 80307-3000

NCSU
Attn J Davis
PO Box 8208
Raleigh NC 27650-8208

Distribution

NTIA ITS S3
Attn H J Liebe
325 S Broadway
Boulder CO 80303

Pacific Missile Test Ctr Geophysics Div
Attn Code 3250
Point Mugu CA 93042-5000

Army Rsrch Laboratory
Attn AMSRL-BE-S Battlefield Envir Dir
Attn AMSRL-BE-W
White Sands Missile Range NM 88002-5501

US Army Rsrch Lab
Attn AMSRL-CI-LL Tech Lib (3 copies)
Attn AMSRL-CS-AL-TA Mail & Records
Mgmt
Attn AMSRL-CS-AL-TP Techl Pub (3 copies)
Attn AMSRL-IS-EE D K Wilson (15 copies)
Attn AMSRL-SE-EE Z G Sztankay
Adelphi MD 20783-1197

REPORT DOCUMENTATION PAGE			Form Approved OMB No. 0704-0188	
Public reporting burden for this collection of information is estimated to average 1 hour per response, including the time for reviewing instructions, searching existing data sources, gathering and maintaining the data needed, and completing and reviewing the collection of information. Send comments regarding this burden estimate or any other aspect of this collection of information, including suggestions for reducing this burden, to Washington Headquarters Services, Directorate for Information Operations and Reports, 1215 Jefferson Davis Highway, Suite 1204, Arlington, VA 22202-4302, and to the Office of Management and Budget, Paperwork Reduction Project (0704-0188), Washington, DC 20503.				
1. AGENCY USE ONLY (Leave blank)		2. REPORT DATE July 1997		3. REPORT TYPE AND DATES COVERED Final, 1 May 1996 to 14 June 1996
4. TITLE AND SUBTITLE Performance of Acoustic Tracking Arrays in Atmospheric Turbulence			5. FUNDING NUMBERS DA PR: B53A PE: P61102	
6. AUTHOR(S) David Keith Wilson				
7. PERFORMING ORGANIZATION NAME(S) AND ADDRESS(ES) U.S. Army Research Laboratory Attn: AMSRL-IS-EE 2800 Powder Mill Road Adelphi, MD 20783-1197			8. PERFORMING ORGANIZATION REPORT NUMBER ARL-TR-1286	
9. SPONSORING/MONITORING AGENCY NAME(S) AND ADDRESS(ES) U.S. Army Research Laboratory 2800 Powder Mill Road Adelphi, MD 20783-1197			10. SPONSORING/MONITORING AGENCY REPORT NUMBER	
11. SUPPLEMENTARY NOTES AMS code: 611102.53A11 ARL PR: 7FEJ60				
12a. DISTRIBUTION/AVAILABILITY STATEMENT Approved for public release; distribution unlimited.			12b. DISTRIBUTION CODE	
13. ABSTRACT (Maximum 200 words) <p>A method is described for assessing the performance of acoustic arrays used to determine source bearings. The method involves calculation of the Cramer-Rao lower bound (CRLB), which characterizes the best performance obtainable for a given array configuration and set of operating conditions. The CRLB calculations are used to show that the performance of the arrays depends on the sensor configuration, the acoustic frequency, the distance from the source, the background noise, and atmospheric turbulence. Near to the source, and at low frequencies, it is the background noise that limits array performance. Turbulence becomes the limiting factor as the distance and frequency are increased. When performance is limited by turbulence, the calculations are found to be very sensitive to the particular turbulence model used. The von Kármán type of model appears to provide the most reasonable CRLB calculations. The turbulent degradation is found to result primarily from small-scale fluctuations in the wind velocity. Performance predictions for ARL's Remote Netted Acoustic Detection System (RNADS) are presented; it is found that RNADS should provide angle-of-arrival (AOA) accuracy of several degrees or better for signal-to-noise ratios above 10 dB during most atmospheric turbulence conditions.</p>				
14. SUBJECT TERMS Acoustic arrays, turbulence, acoustic propagation			15. NUMBER OF PAGES 48	
			16. PRICE CODE	
17. SECURITY CLASSIFICATION OF REPORT Unclassified	18. SECURITY CLASSIFICATION OF THIS PAGE Unclassified	19. SECURITY CLASSIFICATION OF ABSTRACT Unclassified	20. LIMITATION OF ABSTRACT UL	